Check for updates

Electrospun carbon nanodot-doped PVDF nanofibers with enhanced crystallinity, hydrophobicity and UV resistance

Ahmad Hamisu, [ID] [ab] Shittu Abdullahi, [ID] *[cd] Ahmed Alshahrie[a] and Numan Salah*[b]

PVDF is known to be synthesized into nanofibers for various applications, including wastewater treatment through oil–water separation, adsorption, and filtration. However, long-term stability and fouling remain significant shortcomings. In this study, low-cost, steam-activated date palm fronds carbon nanodots (DPF CNDs) derived from natural sources were incorporated into polyvinylidene fluoride (PVDF) nanofiber mats at varying concentrations ranging from 0 to 5 wt%. We investigated the impact of CNDs loading on surface morphology, wettability, crystalline structure, thermal stability, mechanical properties, and UV resistance. We found that α-phase crystallinity increased with increasing CND concentration; the membranes also exhibited thermal stability, with a slightly decreasing melting temperature. Additionally, a slight decrease in tensile strength was observed with increasing elongation at break, as measured by mechanical testing, indicating improved flexibility. Enhanced hydrophobicity was also observed, as evidenced by a higher contact angle that remained stable after UV exposure, thereby demonstrating improved UV resistance. Therefore, these CND-doped PVDF nanofibers demonstrated potential for antifouling applications, particularly in the adsorption of organic pollutants and oil–water separation.

Introduction

Nanofibers are tiny fibrous materials with diameters typically ranging from 1 to 100 nm and a high aspect ratio. Depending on their intended use, they can be made from organic polymers or inorganic materials.[1] Nanofibers have become increasingly important in various fields thanks to their high surface area, porosity, and tunable structure. These include environmental cleanup (such as wastewater treatment, oil–water separation, and pollutant adsorption), biomedical applications (like drug delivery and tissue engineering), and energy devices.[2–7] Polymer-based nanofibers are especially attractive because they are environmentally friendly, biocompatible, flexible, recyclable, and amenable to chemical modification. These properties make them versatile in technologies ranging from water treatment to sensors and piezoelectric devices.[8,9]

There are several methods for producing nanofibers, including phase separation, template synthesis, and mechanical drawing. However, electrospinning and electro-spraying are yet the most efficient and widely used techniques for transforming many raw materials for different functional applications.[10] Electrospinning has progressed from a single-fluid mixing technique[11] to coaxial,[12] side-by-side,[13] triaxial,[14] tri-fluid side-by-side,[15] and other complicated processes.[16] However, these methods, such as single-fluid blending electrospinning, endow the nanofibers with active chemicals that dictate their intended functional applications. Electrospinning is relatively simple, cost-effective, and allows precise control over fiber morphology. Electrospun nanofibers are well-known for their good crystallinity, high surface area, uniform structure, and porosity, making them ideal for filtration, electronics, catalysis, and biomedicine.[17,18] PVDF is one of the most commonly used electrospun polymers, primarily due to its chemical resistance, thermal stability, and piezoelectric properties.[19] PVDF exists in different crystalline phases, with the most common ones being the nonpolar α-phase and the polar β-phase. The α-phase provides hydrophobicity and structural stability, which is beneficial for filtration and separation applications. On the other hand, the β-phase offers piezoelectric properties that are more relevant to sensors and energy harvesting devices.[19,20]

Thanks to its hydrophobic nature, often characterized by a water contact angle close to 120°, PVDF electrospun nanofibers have been effectively used to separate oil from water and adsorb organic pollutants.[21] However, fouling is one of the biggest challenges in using PVDF membranes for water treatment.[22–24] Over time, contaminants accumulate on the membrane surface, reducing performance.[20] However, chemical cleaning and

[a]*Department of Physics, Faculty of Sciences, King Abdulaziz University, Jeddah-21589, Saudi Arabia*

[b]*Center of Nanotechnology, King Abdulaziz University, Jeddah-21589, Saudi Arabia*

[c]*Department of Pure and Applied Physics, Faculty of Science, Gombe State University, P.M.B. 127, Gombe, Nigeria*

[d]*Nuclear Science Program, Department of Applied Physics, Faculty of Science and Technology, Universiti Kebangsaan Malaysia (UKM), Bangi 43600, Selangor, Malaysia*

backwashing are standard cleaning methods. But these cleaning methods can damage the membrane, especially when harsh chemicals are involved.[21] To address this issue, researchers have modified PVDF by coating its surface with more hydrophilic materials or blending it with other polymers or nano-materials.[25,26] Some studies have introduced polymers such as PAN, PVA, and PMMA[27,28] or nanomaterials like graphene oxide, titanium dioxide, and cellulose nanocrystals.[29,30] These additives help to improve wettability and reduce fouling.[31] However, they can also be expensive and difficult to disperse uniformly in the PVDF matrix. While several carbon-based nanofillers, such as graphene, graphene oxide, and carbon nanotubes, have been used to modify PVDF membranes.[29,30]

Many of these additives tend to enhance the β-phase and modify surface wetting behavior, which may not be ideal for improving fouling resistance. Additionally, high cost, dispersion uniformity, and long-term UV stability can limit their practical applicability. For example, CNTs and graphene, with their large aspect ratios and electronic structures, when well-dispersed, serve as nucleation sites in polymers, promoting the all-trans (TTTT) conformation of the β-phase in PVDF. Furthermore, their electrical conductivity enhances fiber alignment and crystallinity by amplifying the local field during electrospinning. This reduces its surface energy, thereby increasing its hydrophobicity. GO particles, in addition, when uniformly dispersed within the PVDF matrix, enhance its alpha-to-beta phase transition due to the GO crystal lattice matching with the PVDF β-phase. However, this also increases the surface energy and decreases the hydrophobicity of the PVDF due to the hydrophilic nature of GO.[32] When steam-activated CNDs are uniformly dispersed within the PVDF matrix, they inhibit nucleation and alter polymer chain alignment during electrospinning.[33] This favors the T-*trans*, G-*gauche*⁺, G′-*gauche*-dihedral (TGTG′) conformation of the α-phase, which is responsible for PVDF's hydrophobic properties. Despite their high surface area and porosity, which may retain water *via* capillary, steam-activated CNDs have rougher surfaces and fewer oxygenated groups than GO, making them less hydrophilic.[34]

On the other hand, steam-activated CNDs derived from renewable biomass, particularly date palm fronds, are a sustainable and scalable alternative. These steam-activated CNDs are low-cost, highly crystalline, and exhibit excellent dispersion in polymer matrices without requiring surface functionalization.[35,36] Moreover, these steam-activated CNDs were reported to have efficiently removed organic pollutants from water with high precision.[36] Despite their promise, their influence on PVDF nanofibers, particularly in terms of crystallinity, wetting behavior, UV resistance, and fouling mitigation, remains underexplored. In this study, we incorporate steam-activated CNDs into PVDF electrospun nanofibers at varying concentrations and evaluate their effects on surface morphology, crystalline structure, thermal behavior, mechanical properties, and surface wettability. Our goal is to assess their potential to enhance membrane properties relevant to their performance for applications such as the removal of organic pollutants as well as oil–water mixture separation in wastewater treatment.

Materials and methods

Materials

PVDF (M_w ~534 000 by GPC) powder and high-purity *N,N*-dimethylformamide (DMF) were purchased from Sigma-Aldrich. CNDs were sourced from date palm fronds using a ball milling technique as previously described.[35,37,38] Before the electrospinning process, polymeric solutions of different CNDs concentrations, namely, 0 wt%, 1.25 wt%, 2.5 wt%, and 5 wt%, were made by dissolution of the PVDF powder in DMF under constant stirring at 65–70 °C for 3–4 h until a homogeneous polymeric solution is achieved, after which the CNDs powder was added and kept under continuous stirring overnight at 50 °C to allow for better CNDs dispersion in the polymer matrix.

Methods

Production and activation of CNDs. The date palm frond CNDs were fabricated following the method described previously.[38,39] The CNDs were fabricated by first cutting dried date palm fronds into small pieces, washing them with water, and then drying them in a furnace overnight. The dried date palm fronds were subsequently carbonized at 350 °C in an oven for 3 hours. The carbon nanostructures from carbonized date palm fronds were produced using the ball-milling technique, in which the moving balls, upon collision, transfer mechanical energy to the carbon materials within the milling jars, thereby crushing the larger carbonized date palm fronds into carbon nanostructures. After ball milling, the CND sample is physically activated with steam as the gasifying agent under a nitrogen atmosphere at 800 °C for 60 minutes.

Electrospinning. Electrospinning is a parameter-driven process; in other words, the nature and features of the resulting electrospun nanofibers are based solely on the parameters and electrospinning conditions employed during the process.[40] These parameters and conditions include the polymer solution's composition, the solvent's nature, the feed rate, the distance between the needle tip and the collector, the spinneret width and speed, the applied voltage, the temperature, and the atmospheric conditions of the electrospinning environment. Based on the preferred application, the properties of PVDF-based electrospun nanofibers, including their morphologies, crystallization phases, and piezoelectrical properties, can be tuned by simply controlling the electrospinning parameters.[41] Consequently, this study examines the effect of incorporating CNDs on the physical, thermal, mechanical, and wetting characteristics of PVDF electrospun nanofibers, while maintaining constant electrospinning parameters and conditions throughout the process.

After cooling, the polymer solution was cooled to room temperature, sonicated for 30 minutes, and then transferred into a 10 mL syringe. A small-diameter tube was attached to the filled syringe at one end using a plastic-and-metal connector with a needle on the other end. Finally, the filled syringe was fixed on a holder. The needle is mounted on the electrospinning machine's spinneret. A flat, rectangular glass substrate wrapped in aluminum foil is used as a collector to collect electrospun
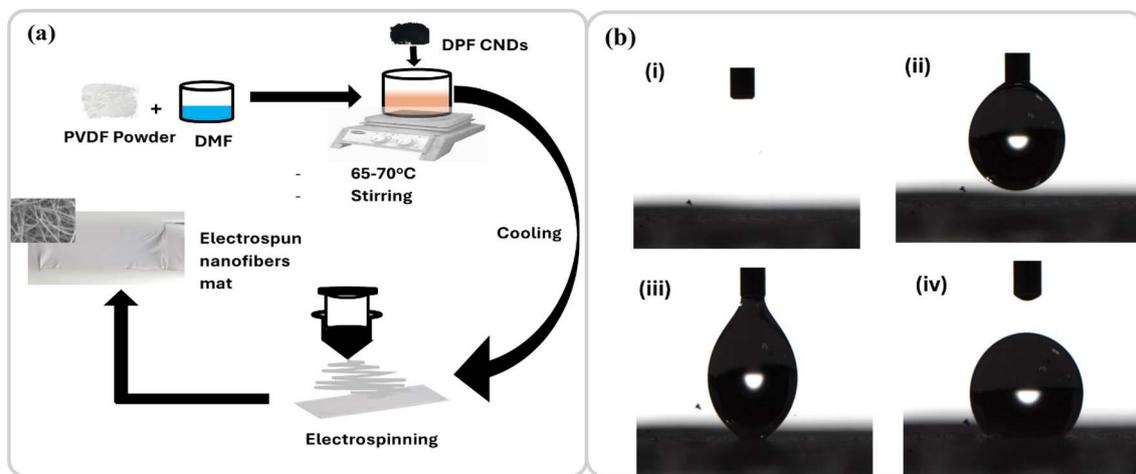
Fig. 1 (a) Electrospinning process, (b) contact angle measurement stages, (i) surface focus, (ii) liquid drop, (iii) contact, (iv) lift-up.

fibers, as shown in Fig. 1a. Table 1 shows the summary of the optimized electrospinning parameters employed during the electrospinning process, which are obtained after several trials of the ranges of feed rate (0.1–0.5 mL h^{-1}), needle tip-collector distance (100–150 mm), spinneret width (120–150), and applied voltage (20–30 kV).

Samples characterizations. The produced DPF CND nanoparticles are studied using a scanning electron microscope (SEM) (JSM-7500 JEOL, Japan) at 5.0 kV. The transmission electron microscopy (TEM) images of the CNDs samples were taken by employing the same procedure reported previously.[42] The high-resolution transmission electron microscopy (HRTEM) images were obtained using a JEOL JEM-2100F (Japan). The Raman spectrum was obtained using the DXR Raman spectroscope, while the surface chemistry was examined with X-ray photoelectron spectroscopy (XPS) (PHI5000 VersaProbeII, Japan).

The morphology of the electrospun nanofiber samples was evaluated using the SEM machine mentioned above under the same operating conditions. The average nanofiber diameter is estimated using the free online ImageJ software package developed by the National Institutes of Health, USA. The crystallographic structures of the nanofiber samples were studied using an Ultima-IV X-ray diffractometer with an operating voltage of 40.0 kV, a current of 30.0 mA, and a Cu Kα X-ray wavelength of 1.5418 Å. Other employed operating parameters are an angular interval of 5 to 90°, a step range of 0.02°, and a Div Slit of 2/3°. On the other hand, the phase composition of the prepared nanofiber samples was investigated using a DXR Raman spectroscope with

a 6 mW source power and a 532 nm laser. On the other hand, the thermal characteristics of the nanofiber samples were evaluated using a differential scanning calorimeter incorporated thermogravimetric analyzer (TGA-1550, Bioevopeak Co., Ltd., China) at a heating rate of 10 °C min^{-1} in the temperature range of 30–300 °C under an air atmosphere.

Contact angle measurements. The wetting properties of the electrospun nanofiber samples were examined using a sessile drop contact angle measurement setup, with water and olive oil as the test liquids. The fiber sample on a substrate is placed on the sample holder, and the sample surface image is monitored and displayed on the computer monitor screen connected to the setup. Four microliters of water/oil droplets are dropped on the fiber sample's top layer, and the contact angle between the water droplet and the nanofiber surface is carefully measured. The contact angle measurement stages are illustrated in Fig. 1b.

Nanofibers UV-irradiation. The prepared nanofiber samples were subjected to UV radiation for 15, 30, and 60 minutes using a high-intensity UV irradiation SPDI UV Exposure Lab Chamber (UVB = 280 nm; model number 800.977.7292). The samples were irradiated at a distance of 6 mm from the light source.[43,44] After UV radiation exposure, we measured the water and oil contact angles on individual samples to investigate their effect.

Nanofibers mechanical properties evaluation. The nanofibers' mechanical behavior was tested using a tensile tester (LRX Plus 2011) with a maximum load of 5 kN (1100Ib). The nanofiber mat samples, approximately 50 mm in length, were vertically folded to allow for a reasonable sample width and thickness. We measured all sample parameters before the tensile test at an extension rate of 30 mm min^{-1} and a gauge length of approximately 50 mm.

Results and discussion

Steam-activated CNDs morphology, surface chemistry, and phase composition

Fig. 2a–c shows the surface morphology of the steam-activated DPF CNDs studied using the SEM images at different

Table 1 Electrospinning process parameters

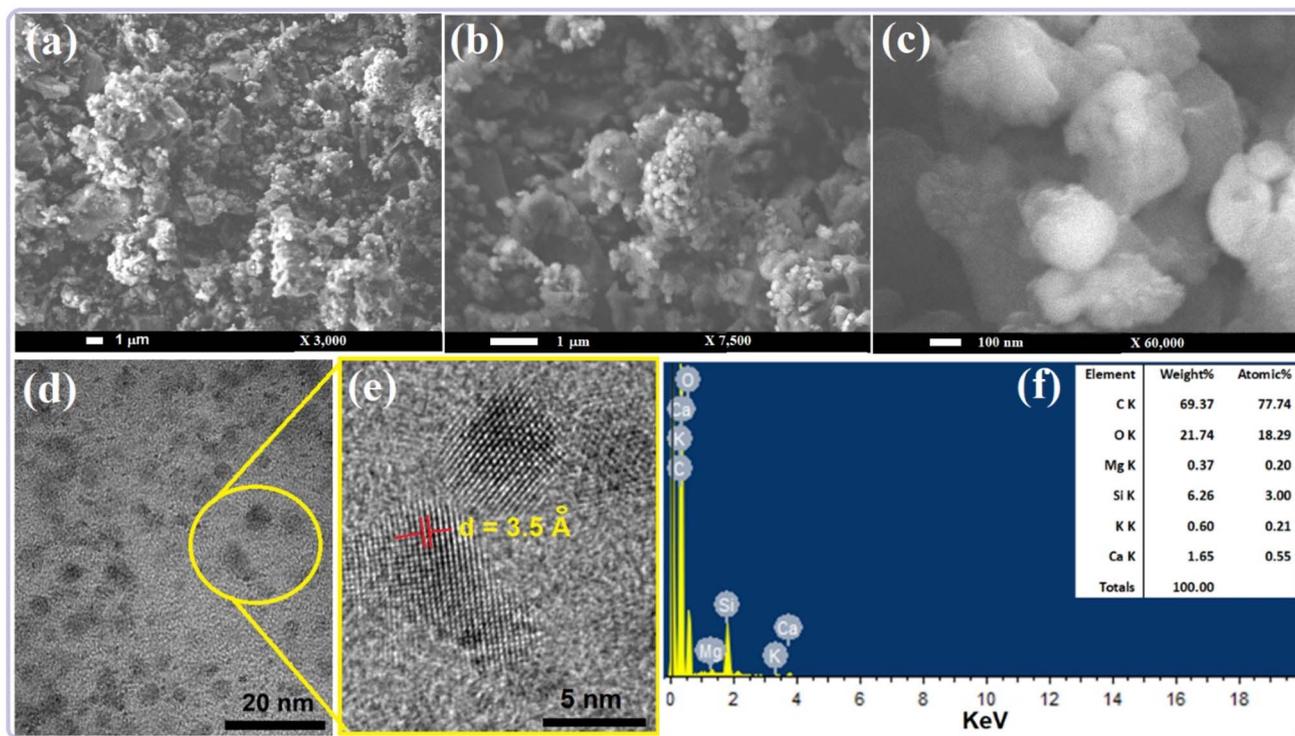| Parameter	Value
Needle tip-collector distance	150 mm
Applied voltage	25 kV
Solution feed rate	0.3 mL h^{-1}
Spinneret width	150 mm
Temperature and humidity	Atmosphere

Fig. 2 (a–c) SEM images at different magnifications, (d) TEM, (e) HRTEM, and (f) EDS analysis of the DPF CNDs.

magnifications. As observed, easily separable agglomerates of nanoscale DPF particles form, with individual particles <100 nm. These agglomerated particles have irregular morphologies, which can improve mesopore formation, as well as surface area, impacting reactivity and adsorption, as reported.[45] The TEM (Fig. 2d) and HRTEM (Fig. 2e) images show, respectively, the ultrafine structures of DPF CNDs nanoparticles. The separated individual CNDs nanoparticles show

highly ordered dots with ~8–10 nm dimensions, having an ~3.50 Å d-spacing which corresponds to the (002) diffraction plane, and show the highly graphitic sp^2 crystalline phase of the CNDs nanoparticles.[45] The presence of some other agglomerates within these images also agrees with the reported results.[46] The EDS quantitative and qualitative analysis (Fig. 2f) shows the elemental composition of the DPF CNDs powder sample with carbon (C) and oxygen (O) together making of up to 91.11% by
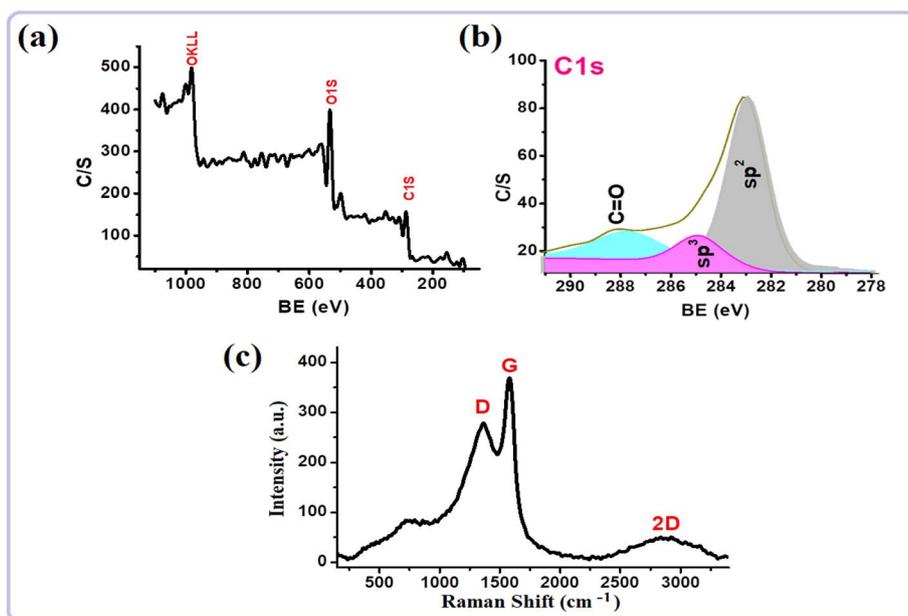

Fig. 3 (a) XPS survey scan curve, (b) XPS spectrum of the C 1s band, and (c) Raman spectrum of the DPF CNDs.

weight, and 96.03% by atom of the total weight and atomic percentages of the sample, indicating higher carbon content with some trace elements of magnesium (Mg), silicon (Si), potassium (K), and calcium (Ca).

Fig. 3a–c shows the XPS survey scan curve, the spectrum of the C 1s band, and the Raman spectrum of the CNDs of the DPF nanoparticles sample. The XPS survey scan curve (Fig. 3a) reveals the presence of carbon and oxygen bands in the DPF CNDs sample. The C 1s band spectrum (Fig. 3b) shows an appearance of sp^2 and sp^3 bands, respectively, at ~283.5 and 285 eV. The sp^2 band intensity was much higher than that of sp^3, which shows a strong graphitic crystalline phase in the DPF CNDs sample. An additional low-intensity band at 288 eV corresponding to functional groups such as C=O is observed.[47] The Raman spectrum (Fig. 3c) shows apparent bands at 1370, 1570, and 2740 cm^{-1}, which correspond to the D-, G-, and 2D-bands, respectively.[48] The D-band represents disordered carbon structure, sp^3 bonding and defects, while the G-band
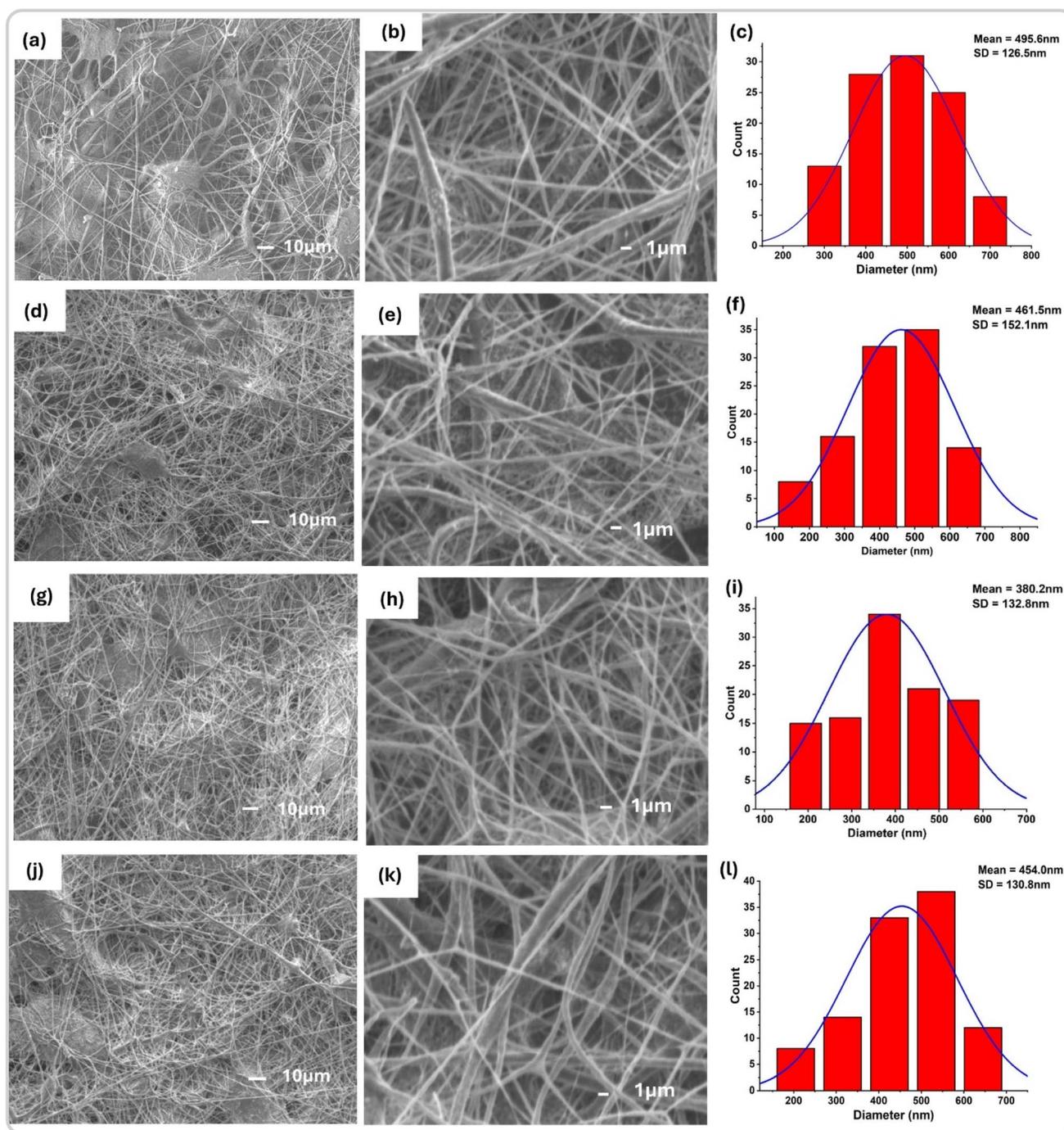

Fig. 4 Low- and high-magnification SEM images; nanofibers diameter distribution of PVDF (a–c), (d–f), PVDF/1.25% CNDs, PVDF/2.5% CNDs (g–i), and PVDF/5% CNDs (j–l) electrospun nanofibers.

signifies graphitic structure, sp^2 bonding and crystalline regularity. The 2D band indicates a graphene-like structure, high regularity, and stacking order.[49,50]

Nanofibers morphology

The morphology and uniformity of the PVDF electrospun nanofibers with an average nanofiber diameter (495.6 ± 126.5
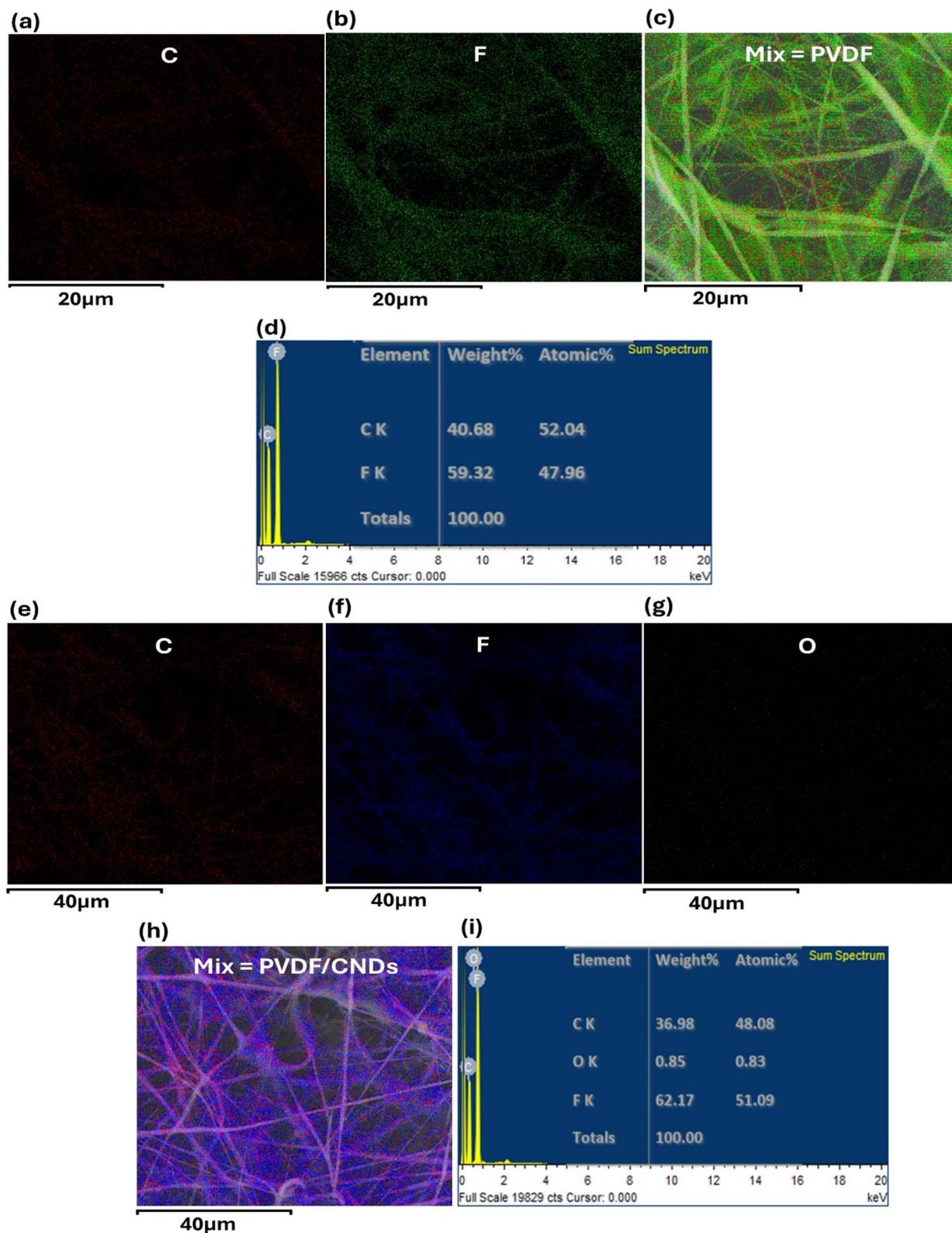

Fig. 5   EDS mapping and spectrum of pure PVDF (a–d), and PVDF/CNDs (e–i) electrospun nanofibers.

nm) (Fig. 4a–c) were observed to improve with 1.25% increased CNDs concentration in the PVDF/CNDs electrospun nanofibers with 461.5 ± 152.1 nm average nanofiber diameter (Fig. 4d–f). Further improvement in the nanofiber morphology, uniformity, as well as the average diameter of (380.2 ± 132 nm) (Fig. 4g–i) is noticed as the CNDs concentration is increased to 2.5% due to the reduction in the polymer solution surface tension and shorter drying period of the electrospun nanofibers as a result of the CNDs presence within the polymer solution. At higher CND concentrations, the nanofibers' morphology tends to decrease slightly, with an average nanofiber diameter of 454 ± 130.8 nm (Fig. 4j–l), resulting from the high viscosity of the polymer solution and a delayed drying period of the resulting electrospun nanofibers. These CND additives at moderate concentration not only improve the morphology, along with the uniformity of the nanofibers' diameter, but also enhance the likelihood of obtaining bead-free nanofibers and the electrospinnability of the PVDF polymer itself.

To address the incorporation and uniformity of CNDs within the produced PVDF nanofibers, we employed energy-dispersive spectroscopy (EDS) mapping, a popular microanalytical method for identifying and quantifying elements in a sample. Fig. 5 shows the EDS mapping and spectrum analysis of the PVDF (a–d) and PVDF/CNDs (e–i) nanofiber samples. It reveals the constituent elements of these electrospun nanofibers and their corresponding atomic and weight percentages. Hence, noticeable incorporation and regular dispersion of the CNDs within the polymer matrix (Fig. 5h: mix = PVDF/CNDs) were achieved successfully. The presence of oxygen and the carbon element, being the central component of CNDs, becomes more visible in Fig. 5h, with transparent red dots/particles in the formed nanofibers.

Nanofibers' crystallinity and thermal stability

Fig. 6a reveals the X-ray diffractograms results of the PVDF and various CNDs concentrations of PVDF/CNDs nanofibers. The nanofiber samples exhibit characteristic diffraction peaks in the 2θ range (15–35°). The PVDF polymer precursor comprises both the alpha and beta crystalline phases. The intensity peaks at 2-theta values of ∼20.28° and 26.54°, corresponding to the (110) and (021) α-phase refraction planes of the PVDF nanofibers, respectively.[51] The intensity peak at 2-theta ∼20.88° corresponds to the combinations of (110 and 200) refraction planes of the β-phase.[51] The β-phase diffraction peak intensity of the PVDF nanofiber is observed to be suppressed upon the introduction of CNDs, due to interactions between the polymer chains and the CNDs within the polymer matrix. The observed increase in the intensity of the α-phase peak at 2θ ∼20.28° and the instability of the 2θ ∼26.54° peak intensity at higher CND concentrations indicate that CND disrupts the crystallinity of the PVDF nanofibers. The increase in the alpha–beta ratio observed at moderate CND concentrations in Fig. 6b provides further evidence of preferential α-phase crystallization. This could be likely facilitated by the amorphous structure and surface chemistry of the incorporated CNDs. These CNDs may disrupt the chain alignment necessary for β-phase formation, thereby stabilizing the thermodynamically favored α-phase. Quantitatively, the increase in the α/β ratio suggests enhanced surface interactions between PVDF chains and the CNDs interfaces. Consequently, the presence of the CNDs at higher concentrations within the PVDF matrix can result in the α/β ratio decrease as well as an overall decrease in the nanofibers' crystallinity as observed in the X-ray diffractograms (Fig. 6a).

The first heating (endothermic) thermogravimetric analysis curves of PVDF and PVDF/CND nanofibers (Fig. 7a) further reveal the thermal characteristics and crystallization behavior of the nanofiber samples. The percentage crystallinity was computed using eqn (1) based on the enthalpy of melting of the individual nanofiber samples, which utilized the reported enthalpy of melting ($\Delta H = 105$ J g^{-1}) of a 100% crystalline PVDF sample.[52] The overall decrease in the melting temperature, from 160.95 °C for PVDF nanofibers to 158.82 °C at higher CND concentrations, indicates a weakening of intermolecular forces due to the introduction of CNDs. Consequently, the melting enthalpy of the PVDF nanofibers (ΔH_m) decreased from 39.60 J g^{-1} to 35.11 J g^{-1}. The percentage of crystallinity (X_c) ranged from 37.82% to 33.53% (at higher CND concentrations), as presented in Table 2. The results indicate the presence of CNDs
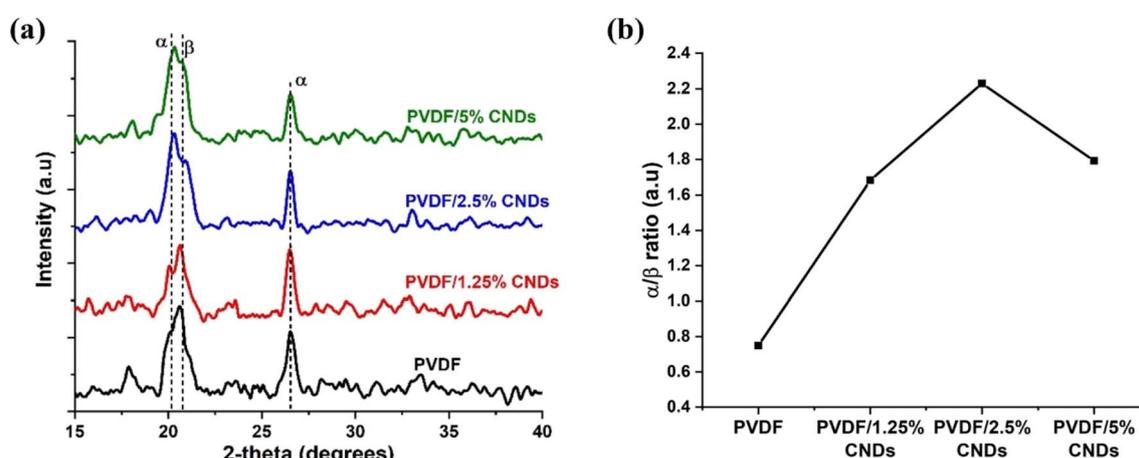

Fig. 6 (a) X-ray diffractograms, and (b) alpha–beta ratio of the PVDF and PVDF/CNDs (with various CNDs concentrations).
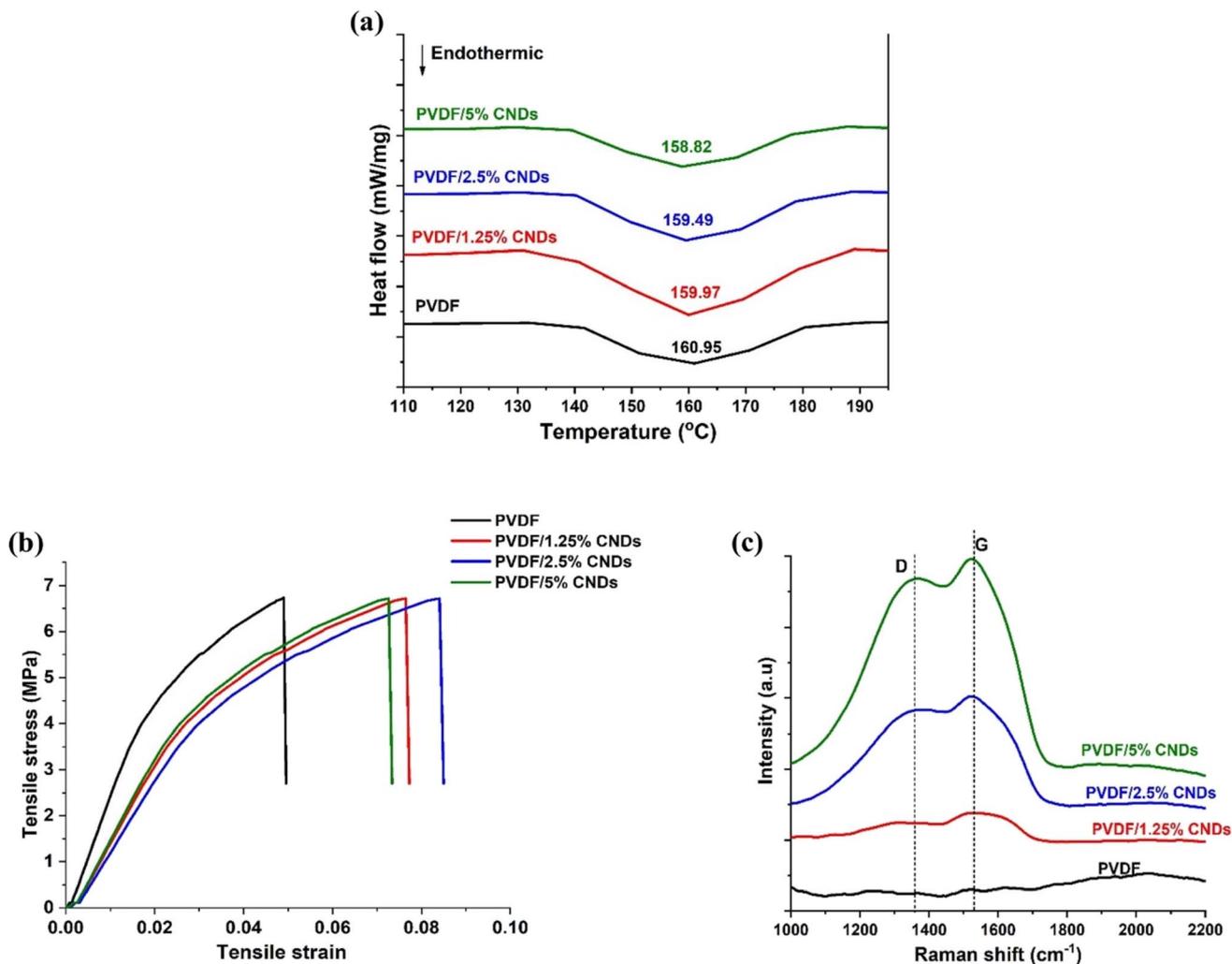
Fig. 7 (a) Thermo-analytical curves; (b) Raman spectra; (c) stress–strain curves of the PVDF and PVDF/CNDs electrospun nanofibers (with various CNDs concentrations).

in the PVDF matrix, which alters the polymer chain alignment due to its amorphous nature.[53] Moreover, the surface charges of the CNDs may also disrupt polymer crystallinity due to the rapid nucleation rate during solidification.[33]

$$\text{Percentage crystallinity,} \quad X \ (\%) = \frac{\Delta H_m}{\Delta H} \times 100 \qquad (1)$$

where ΔH_m and ΔH are the enthalpies of melting of a given sample and a 100% crystalline PVDF sample, respectively.

Table 2 Thermo-analytical data of PVDF and PVDF/CNDs electrospun nanofiber samples with varying CNDs concentrations

Sample	T_m (°C)	ΔH_m (J g^{-1})	X_c (%)
PVDF	160.95	39.60	37.82
PVDF/1.25% CNDs	159.97	37.42	35.74
PVDF/2.5% CNDs	159.49	37.32	35.65
PVDF/5% CNDs	158.82	35.11	33.53

The distinct bands at ~1370 cm^{-1} and 1570 cm^{-1} in the Raman spectra of the PVDF/CNDs electrospun nanofiber samples (Fig. 7b) indicate the presence of CNDs within the PVDF matrix. This band appeared absent from the PVDF nanofiber sample's spectrum. However, it showed a further increase in intensity with the addition of CNDs, indicating successful incorporation and distribution within the PVDF matrix.

Nanofibers' mechanical properties

Fig. 7c below reveals the stress–strain curves of the individual nanofiber mat samples. Pure PVDF nanofibers exhibited a high tensile strength of 6.84 MPa and a relatively low total elongation at fracture. By adding CNDs at different loadings, the tensile strength value remains almost invariant but with an increased elongation at fracture, particularly at a 2.5 wt% CNDs concentration. This increased elongation at fracture may be due to alterations in the polymer's crystal structure resulting from the CNDs' interaction with the polymer chains. This implies that
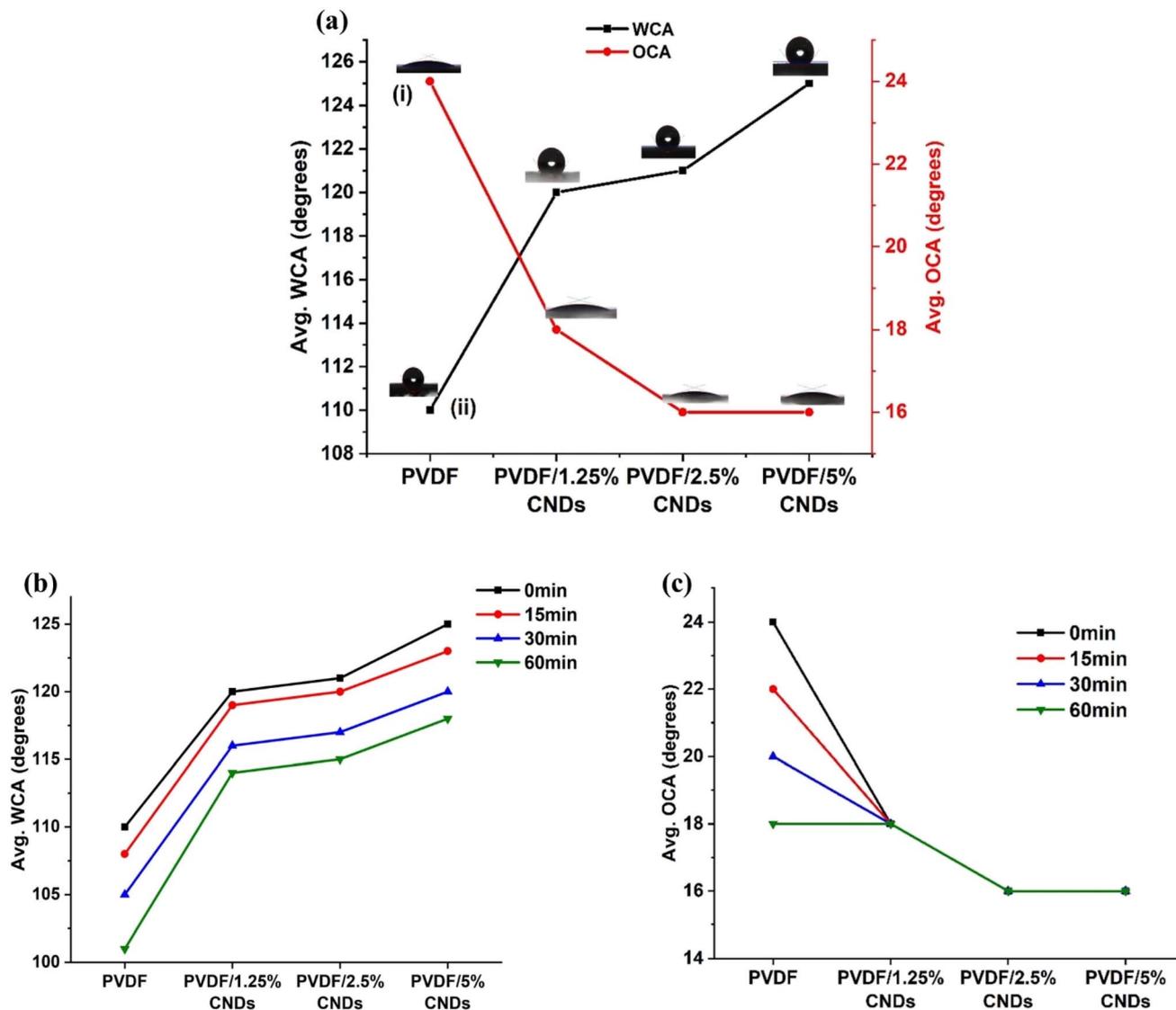
Fig. 8 (a) Average (i) water and (ii) oil contact angles before UV-irradiation; post-UV exposure average (b) water; and (c) oil contact angles of PVDF and PVDF/CNDs electrospun nanofibers (with various CNDs concentrations).

the presence of CNDs at a moderate ratio within the PVDF crystal lattice reduced its crystallinity by breaking the long-range order required for PVDF crystallinity, leading to polymer chain rearrangement and the formation of more amorphous regions. This makes the PVDF nanofibers less crystalline, and so enhances their percentage elongation.[54] Similar behavior involving carbon-based nanomaterials in beta-form PVDF nanocomposites reinforced with CNTs was also reported.[55] The calculated average tensile strength and percentage elongation at fracture from the tensile test data of the nanofiber samples are listed in Table 3 below.

Nanofibers' surface wetting behaviours

Fig. 8a reveals the surface-wetting behavior of the PVDF and PVDF/CNDs electrospun nanofibers. The observed contact angles of (i) water and (ii) oil before UV irradiation are found to vary from $110° \pm 2°$ and $24° \pm 2°$ for the PVDF nanofiber to $125° \pm 2°$ and $16° \pm 2°$ for the PVDF/CNDs nanofiber samples, respectively. In other words, the water contact angle increased by $15°$, representing an approximate 14% increase in hydrophobicity, which is significant for membrane performance.

Table 3 Average tensile strength and percentage elongation at fracture for PVDF and PVDF/CNDs nanofiber samples with varying CNDs concentrations

Sample	Tensile strength (MPa)	Elongation at fracture (%)
PVDF	6.84	4.9
PVDF/1.25% CNDs	6.68	7.6
PVDF/2.5% CNDs	6.66	8.4
PVDF/5% CNDs	6.59	7.2

Furthermore, there is an overall increase in the water contact angles and oleophilicity of PVDF nanofiber samples with increased CNDs concentration due to the decreased surface energy and changes in crystallinity of the nanofibers caused by the CNDs additives.[56] Fouling resistance is related to the crystallinity and hydrophobicity of nanofibers. Hydrophobic, more crystalline nanofibers tend to exhibit stronger fouling resistance than less crystalline ones. Our results show that although a slight reduction in nanofibers' crystallinity is noticed, their enhanced hydrophobicity can make them more resistant to fouling.

After the different UV-irradiation periods, the water contact angles on the sample surface were found to vary from $110 \pm 2°$ to $101 \pm 2°$ for the PVDF nanofibers and $125 \pm 2°$ to about $118 \pm 2°$ for the PVDF/CNDs nanofiber samples (Fig. 8b). This indicates that, compared with the PVDF nanofiber sample, UV radiation does not significantly affect the water contact angle of the PVDF/CNDs nanofibers, suggesting enhanced UV resistance of PVDF due to the CNDs additives. This was further observed by examining the UV-irradiated samples by determining the oil contact angle on the surface of the sample, which shows a slight variation from $24° \pm 2°$ to about $18° \pm 2°$ for the PVDF nanofiber sample and relatively less or no change in the oil contact angle of the PVDF/CNDs nanofiber samples with different CNDs concentrations (Fig. 8c). The lack of or minimal effect of UV-radiation on the surface wetting behavior of PVDF and PVDF/CND nanofiber samples is attributed to the improved UV-radiation resistance of CNDs on the PVDF itself. This agrees with the CNDs and PVDF polymer UV-resistance ability reported in the previous studies.[57]

From an application perspective, the information obtained provides insight into the development of antifouling PVDF electrospun nanofibrous membranes incorporating steam-activated CNDs. This approach will certainly help to produce nanofibers with enhanced antifouling properties, UV radiation resistance, and excellent adsorption capacity for organic pollutants, as well as separation capabilities for oil/water mixtures in laboratory and industrial wastewater treatment applications.

Conclusions

In this study, we reported the successful infusion of steam-activated carbon nanodots into PVDF electrospun nanofibers using a scalable and straightforward process. The synthesized nanofibers exhibited improved hydrophobicity with up to a 14% increase in their WCA, enhanced surface morphology and uniformity as seen in the SEM images, increased α/β ratio and percentage elongation at moderate concentrations, and superior resistance to UV-induced degradation. These attributes directly address key limitations of traditional PVDF membranes, particularly in antifouling and UV-exposed environments. Compared to other nanofillers reported in the literature, our approach provides a low-cost, bio-derived, and effective method for enhancing PVDF performance for possible wastewater treatment applications.

Author contributions

Ahmad Hamisu: conceptualization, data curation, investigation, methodology, writing – original draft. Shittu Abdullahi: visualization, investigation, data curation, writing – review and editing. Ahmed Alshahrie: supervision, investigation, resources. Numan Salah: supervision, conceptualization, validation, writing – review and editing, resources.

Conflicts of interest

There are no conflicts to declare.

Data availability

All data supporting the findings of this study are available within the manuscript. The raw datasets generated and analyzed during the current study are provided in the supplementary information (SI). Supplementary information: provides all raw data supporting the figures in the manuscript, ensuring full transparency and reproducibility of the results. It also includes additional experimental details, characterization data, and further supporting details that were not included in the main text. See DOI: **https://doi.org/10.1039/d5ra06847a**.

Acknowledgements

Notes and references

1 A. A. Altaf, M. Ahmed, M. Hamayun, S. Kausar, M. Waqar and A. Badshah, *Inorg. Chim. Acta*, 2020, **501**, 119268.
2 M. T. Abdu, K. A. Abuhasel, M. Alquraish, S. Nagy, S. Khodir and A. A. Ali, *J. Polym. Res.*, 2023, **30**, 340.
3 Y. H. Teow, B. S. Ooi, A. L. Ahmad and J. K. Lim, *Membranes*, 2020, **11**, 16.
4 L. L. Hui Ting, Y. H. Teow, E. Mahmoudi and B. S. Ooi, *Sep. Purif. Technol.*, 2023, **305**, 122428.
5 M. Shigrekar and V. Amdoskar, *RSC Adv.*, 2024, **14**, 32668–32699.
6 C. Bahloul, S. Ez-Zahraoui, A. Eddiai, O. Cherkaoui, M. Mazraoui, F. Z. Semlali and M. El Achaby, *RSC Adv.*, 2024, **14**, 38872–38887.
7 F. Zainab, A. Aftab, S. Mir, N. S. Awwad and H. A. Ibrahium, *RSC Adv.*, 2025, **15**, 36670–36703.
8 Y. Du, Y. Li and T. Wu, *RSC Adv.*, 2017, **7**, 41838–41846.
9 G. Hernández, T. K. Lee, M. Erdélyi, D. Brandell and J. Mindemark, *J. Mater. Chem. A*, 2023, **11**, 15329–15335.
10 B. Ding, C. Kim, H. Kim, M.-K. Seo and S.-J. Park, *Fibers Polym.*, 2004, **5**, 105–109.
11 Y. Chen, W. Gong, Z. Zhang, J. Zhou, D.-G. Yu and T. Yi, *Int. J. Mol. Sci.*, 2024, **25**, 9524.

12 R. Dong, W. Gong, Q. Guo, H. Liu and D.-G. Yu, *Polymers*, 2024, **16**, 2614.

13 D.-G. Yu, W. He, C. He, H. Liu and H. Yang, *Nanomedicine*, 2025, **20**, 271–278.

14 Y. Hu, F. Zhang, J. Zhou, Y. Yang, D. Ding, M. Li, C. Wang, B. Wang, J. Yu, F. Jiang, D. Yu and H. Shen, *Small*, 2025, **21**(42), e05523.

15 D.-G. Yu and J. Zhou, *Next Mater.*, 2024, **2**, 100119.

16 W. Wang, X. Yang, H. Yin, Y. Lu, H. Dou, Y. Liu and D. Yu, *Macromol. Rapid Commun.*, 2025, **46**(10), 2401152.

17 B. Danagody, N. Bose and K. Rajappan, *J. Polym. Res.*, 2024, **31**, 119.

18 W. Zhang, Z. He, Y. Han, Q. Jiang, C. Zhan, K. Zhang, Z. Li and R. Zhang, *Composites, Part A*, 2020, **137**, 106009.

19 O. N. Alqallab and M. H. Hj Jumali, *Polymer*, 2024, **304**, 127137.

20 T. A. Otitoju, A. L. Ahmad and B. S. Ooi, *J. Water Proc. Eng.*, 2016, **14**, 41–59.

21 Z. Zhu, L. Wang, Y. Xu, Q. Li, J. Jiang and X. Wang, *J. Colloid Interface Sci.*, 2017, **504**, 429–439.

22 R. Mohamat, A. B. Suriani, A. Mohamed, Muqoyyanah, M. H. D. Othman, R. Rohani, M. H. Mamat, M. K. Ahmad, M. N. Azlan, M. A. Mohamed, M. D. Birowosuto and T. Soga, *Int. J. Environ. Res.*, 2021, **15**, 149–161.

23 M. A. Ahmad, B. S. Zainal, N. H. Jamadon, T. C. S. Yaw and L. C. Abdullah, *J. Water Reuse Desalin.*, 2020, **10**, 187–199.

24 A. James, M. R. Rahman, K. A. bin Mohamad Said, M. Namakka, M. Shahabuddin, M. S. M. Al-Saleem, J. Y. Al-Humaidi, M. M. Rahman and M. A. Salam, *RSC Adv.*, 2025, **15**, 31471–31497.

25 N. Salim, A. Siddiqa, S. Shahida and S. Qaisar, *Madridge J. Nanotechnol. Nanosci.*, 2019, **4**, 139–147.

26 J. Bose, L. Marchio, U. Adhikari, D. Datta and J. Sikder, *J. Polym. Res.*, 2023, **30**, 246.

27 I. Sriyanti, M. Almafie, R. Dani, M. Idjan, R. Partan, M. Sanjaya and J. Jauhari, *Jur. Penelit. Pendidik. IPA*, 2023, **9**, 7159–7169.

28 J. Xia, Z. Zheng and Y. Guo, *Composites, Part A*, 2022, **157**, 106914.

29 D. Aydemir, E. Sözen, I. Borazan, G. Gündüz, E. Ceylan, S. K. Gulsoy, A. Kılıç-Pekgözlü and T. Bardak, *Cellulose*, 2023, **30**, 885–898.

30 C. Du, Z. Wang, G. Liu, W. Wang and D. Yu, *Colloids Surf., A*, 2021, **624**, 126790.

31 J. Kujawa, S. Boncel, S. Al-Gharabli, S. Koter, W. Kujawski, K. Kaneko, K. Li, E. Korczeniewski and A. P. Terzyk, *Desalination*, 2024, **574**, 117277.

32 Q. Wang, Z. Shao, J. Jiang, Y. Liu, X. Wang, W. Li and G. Zheng, *Nanomaterials*, 2022, **12**, 3115.

33 C. Gong, H. Liu, B. Zhang, G. Wang, F. Cheng, G. Zheng, S. Wen, Z. Xue and X. Xie, *J. Membr. Sci.*, 2017, **535**, 113–121.

34 S. M. A. Abuabdou, Z. H. Jaffari, C.-A. Ng, Y.-C. Ho and M. J. K. Bashir, *Water*, 2021, **13**, 2282.

35 H. Hussain, A. Jilani, N. Salah, A. Memić, M. Omaish Ansari and A. Alshahrie, *Inorg. Chem. Commun.*, 2023, **152**, 110667.

36 N. Salah, S. Abdullahi, M. O. Ansari, A. Hamisu, Y. N. Salah, A. Alshahrie, A. Jelani, A. Memic, and J. Iqbal, *US Pat.* US20250230065A1, 2025.

37 H. Hussain, A. Jilani, N. Salah, A. Memić, M. O. Ansari and A. Alshahrie, *Water Environ. Res.*, 2024, **96**, 11038.

38 N. A. A. Salah, Y. N. A. Salah, A. S. A. Alshahrie, *US Pat.* US010906812B1, 2021.

39 S. M. U. G. Mohiuddin, A. Aydarous, A. Alshahrie, A. Saeed, A. Memić, S. Abdullahi and N. Salah, *RSC Adv.*, 2022, **12**, 27411–27420.

40 I. Y. Abdullah, M. Yahaya, M. H. H. Jumali, and H. M. Shanshool, in *AIP Conference Proceeding*, American Institute of Physics, 2017, p. 1838.

41 S. Aghayari, *Heliyon*, 2022, **8**, e11620.

42 N. Salah, H. Hussain, M. O. Ansari and S. A. Bakar, *J. Taiwan Inst. Chem. Eng.*, 2026, **178**, 106375.

43 S. Abdullahi, A. Aydarous, A. Saeed and N. Salah, *Opt. Mater.*, 2022, **128**, 112402.

44 S. Abdullahi, A. Alshahrie, A. F. Ismail and N. Salah, *RSC Adv.*, 2025, **15**, 26567–26582.

45 R. Khan, S. Bhadra, S. Nayak, A. Bindu, A. A. Prabhu and S. Sevda, *J. Taiwan Inst. Chem. Eng.*, 2024, **165**, 105748.

46 M. Sribalaji, B. Mukherjee, S. R. Bakshi, P. Arunkumar, K. Suresh Babu and A. K. Keshri, *Composites, Part B*, 2017, **123**, 227–240.

47 Y. Qiu, Z. Wang, M. Jin, J. Chen, C. Miao, S. Zhang and L. Lai, *Electrochim. Acta*, 2022, **424**, 140622.

48 K. Y. Aung, Q. Li, F. Chen and M. Wei, *J. Taiwan Inst. Chem. Eng.*, 2025, **176**, 106306.

49 B. G. daFonseca, S. S. Thind, I. Booth and A. G. Brolo, *J. Raman Spectrosc.*, 2024, **55**, 15–25.

50 C. Zhang, J. Jiang, Z. Guan, Y. Zhang, Y. Li, B. Song, W. Shao and L. Zhen, *Advanced Science*, 2024, **11**, e2306159.

51 N. Ahbab, S. Naz, T. B. Xu and S. Zhang, *Micromachines*, 2025, **16**, 386.

52 Z. Fan, M. Schwedes, J. Schwaderer, S. Beuermann and M. Fischlschweiger, *Mater. Res. Lett.*, 2022, **10**, 271–277.

53 M. Nasir, P. P. Puspa Asri and R. I. Sugatri, *IOP Conference Series: Earth and Environmental Science*, Institute of Physics Publishing, 2020, vol. 426, p. 012060.

54 S. A. Habeeb, B. A. Nadhim, B. J. Kadhim, M. S. Ktab, A. J. Kadhim and F. S. Murad, *Adv. Polym. Technol.*, 2023, **2023**, 1–12.

55 M. L. Cerrada, J. Arranz-Andrés, A. Caballero-González, E. Blázquez-Blázquez and E. Pérez, *Polymers*, 2023, **15**, 1491.

56 X. Wang and Q. Zhang, *Powder Technol.*, 2020, **371**, 55–63.

57 M. S. Swapna, C. Beryl, S. S. Reshma, V. Chandran, V. S. Vishnu, P. M. Radhamany and S. Sankararaman, *Bionanoscience*, 2017, **7**, 583–587.